Short Communication

A functional connection between dyskerin and energy metabolism

Alberto Angrisani[a,*], Nunzia Matrone[a], Valentina Belli[b,1], Rosario Vicidomini[a,2], Nunzia Di Maio[a], Mimmo Turano[a], Filippo Scialò[c], Paolo Antonio Netti[b,d], Antonio Porcellini[a], Maria Furia[a,d,*]

[a] Department of Biology, University of Naples "Federico II", Complesso Universitario Monte Santangelo, via Cinthia, 80126 Napoli, Italy
[b] Istituto Italiano di Tecnologia, IIT@CRIB, Largo Barsanti e Matteucci 53, 80125 Napoli, Italy
[c] Institute for Cell and Molecular Biosciences, Campus for Ageing and Vitality, University of Newcastle, Newcastle-upon-Tyne NE4 5PL, United Kingdom
[d] Centro di Ricerca Interdipartimentale sui Biomateriali CRIB, Università di Napoli Federico II, Piazzale Tecchio 80, 80125 Napoli, Italy

ABSTRACT

The human DKC1 gene encodes dyskerin, an evolutionarily conserved nuclear protein whose overexpression represents a common trait of many types of aggressive sporadic cancers. As a crucial component of the nuclear H/ACA snoRNP complexes, dyskerin is involved in a variety of essential processes, including telomere maintenance, splicing efficiency, ribosome biogenesis, snoRNAs stabilization and stress response. Although multiple minor dyskerin splicing isoforms have been identified, their functions remain to be defined. Considering that low-abundance splice variants could contribute to the wide functional repertoire attributed to dyskerin, possibly having more specialized tasks or playing significant roles in changing cell status, we investigated in more detail the biological roles of a truncated dyskerin isoform that lacks the C-terminal nuclear localization signal and shows a prevalent cytoplasmic localization. Here we show that this dyskerin variant can boost energy metabolism and improve respiration, ultimately conferring a ROS adaptive response and a growth advantage to cells. These results reveal an unexpected involvement of DKC1 in energy metabolism, highlighting a previously underscored role in the regulation of metabolic cell homeostasis.

1. Introduction

The human DKC1 gene encodes dyskerin, a highly conserved nuclear protein. Within the nucleus, dyskerin participates in the small nucleolar ribonucleoprotein complexes (snoRNPs), where it binds to H/ACA small nucleolar RNAs (snoRNAs) and acts as a snoRNA-guided pseudouridine synthase, directing the enzymatic conversion of specific uridines to pseudouridines on target RNAs (reviewed by [1]). Dyskerin also participates in the telomerase active complex, contributing to safeguarding telomere integrity [2]. Considering this wide repertoire of essential functions, it is not surprising that DKC1 loss-of-function causes X-linked dyskeratosis congenita and its severe variant Hoyeraal-Hreidarsson syndrome, both characterized by a plethora of disparate symptoms and affecting highly renewing tissues [3–6]. While a large number of studies have deeply investigated the consequences triggered by DKC1 downregulation (reviewed by [5]), to date, little is known about the effects of DKC1 overexpression, despite being well established that it represents a hallmark of many types of sporadic cancers [7–17].

In addition, DKC1 overexpression is associated with resistance to cancer-treating agents and tumor aggressiveness, and is thus considered a marker of poor prognosis [9,14–18]. It is worth noting that DKC1 encodes multiple minor splice isoforms [19,20] whose functions remain poorly understood. In particular, a truncated dyskerin variant that retains intron 12, shows a peculiar cytoplasmic localization and stimulates cell proliferation [19], raising the possibility that it is involved in additional, previously undetermined, biological functions. Consistent with this view, this specific splice variant has recently been related to lipid metabolism [21]. Here we further explored the impact of this dyskerin isoform on cell physiology, and demonstrated that it exhibits new, uncanonical functions; having the ability to promote a metabolic shift that enhances mitochondrial functionality, producing a globally positive impact on oxidative metabolism and conferring a ROS adaptive response and a growth advantage to cells.

---

* Correspondence to: Department of Biology, University of Naples, via Cinthia, 80126 Napoli, Italy.
 E-mail addresses: alberto.angrisani@unina.it (A. Angrisani), mfuria@unina.it (M. Furia).
[1] Present address: Dipartimento Medico-Chirurgico di Internistica Clinica e Sperimentale "F. Magrassi e A. Lanzara. Laboratorio Oncologia Molecolare, Università della Campania Luigi Vanvitelli, Via S. Pansini 5, 80131, Napoli-Italy.
[2] Present address: NICHD (National Institute of Child Health and Human Development)-Section on Metabolic Regulation-NIH-35 Convent DR, Bethesda, MD 20814, USA.

2. Materials and methods

2.1. Cell culture, rotenone and dimethyl malonate treatments

Stably transfected HeLa clones (3XF-Mock, carrying p3XFLAG-CMV-10 empty vector; 3XF-Iso3 expressing the FLAG-tagged Isoform 3) used in these experiments were previously described [19] and cultured in high glucose (4.5 g/l) DMEM medium. For rotenone treatment, cells were exposed overnight to 0.25 μM rotenone (R8875, Sigma-Aldrich, Saint Louis MO) and analyzed by Flow cytometry as described below. For dimethyl malonate (136441, Sigma) treatment, cells were exposed to 100 μM dimethyl malonate for 12 h, and viable cells were counted following 0.4% Trypan Blue (Thermo Fisher Scientific, Waltham, MA) staining. Quiescent cells were obtained by starvation, upon 18 h culture in serum-free medium.

2.2. MTT assay

Reduction of (3-(4,5-Dimethylthiazol-2-yl)-2,5-Diphenyltetrazolium Bromide (MTT) (M2128, Sigma) to formazan salt is dependent on NAD (P)H-dependent cellular oxidoreductases [22] and reflects cell proliferation and metabolic activities. To measure MTT reduction by colorimetric assay, $2.5 * 10^3 - 1 * 10^4$ cells were seeded, in triplicate, in flat bottom 96 wells plates and incubated overnight to allow complete attachment. The following day, cells were washed and incubated for three hours in 100 μl DMEM without phenol red (D2429, Sigma) supplemented with 0.45 mg/ml MTT; the medium was then replaced by 100 μl of 0.1 M HCl in isopropanol and cells were incubated 30 min for lysis. Resuspension of insoluble formazan and following steps were according to MTT manufacturer's protocol. Optical densities were recorded by a Sinergy H4 spectrophotometer (BioTek, Winooski, VT).

2.3. Oxygen consumption measurements

Trypsinized cells were resuspended in PBS at $5 * 10^6$ cells/ml; 10^6 cells were added to 3 ml of fresh DMEM and oxygen consumption rate was recorded by a Clark-type electrode (Yellow Springs Instruments Co., Yellow Springs, OH).

2.4. Immunofluorescence analysis and MitoTracker Green staining

Immunofluorescence microscopy analysis was performed on confluent cells as previously described [19]. Confocal micrographs were taken by either the Zeiss LSM 700 microscope (Zeiss, Oberkochen, Germany), or by the multiphoton Leica TCSSP5 MP (Leica, Solms, Germany), using HC PL IRAPO 40x or 63x water objectives and analyzed by ImageJ software tools [23]. For LUT quantitative analysis, confocal images of 3XF-Iso3 and 3XF-Mock cells were captured using identical filters, laser power and gain settings. The intensity of the fluorescent signals was calculated from total sum of planes. Obtained values were normalized in respect to cell areas (MitoTracker Green and PRDX-2, and reported as Intensity/cell area ratio) or in respect to F-actin signal (TOM20, and reported as TOM20 intensity/actin intensity ratio). To measure mitochondrial mass, live cells were stained with 100 nM MitoTracker Green (M7514, Thermo) for 30 min and confocal pictures were acquired and analyzed as described above. Antibodies used are listed in Appendix A, Supplemental Table 1.

2.5. qPCR and qRT-PCR analysis

DNA and RNA were extracted using TRI Reagent (T9424, Sigma) according to the manufacturer's instructions and quantified by NanoDrop 9000 (Thermo). qRT-PCR experiments aimed at determining PGC1-α and PPRC1 expression in quiescent cells were performed as described in [19]; the HPRT1 and GSS housekeeping genes were used for normalization. For qPCRs, 25 ng total DNA were used. Cycling profile for amplification of 16 S mt-rRNA gene consisted of; one step at 95 °C for 10 min; 40 two-step cycles at 95 °C for 10 s, and at 60 °C for 60 s. In order to avoid underestimation of the mitochondrial DNA content due to eventual degradation, the integrity of total DNA was checked by gel electrophoresis and the length of the amplified fragment was designed to be 136 bp. The following cycling profile was used for amplification of the TSH receptor gene; one step 95 °C for 10 min, 40 three-step cycles at 95 °C for 45 s, at 52 °C for 30 s, and at 72 °C for 35 s. All oligonucleotides were selected using Primer3 software [24] and synthesized on demand by Sigma; their sequences are listed in Appendix A, Supplemental Table 2. For PGC1-α expression analysis, oligonucleotides were derived from regions common to all isoforms.

2.6. Flow cytometry analysis

For TMRE staining, cells were washed three times with PBS, trypsinized and resuspended in staining solution [156 mM NaCl, 3 mM KCl, 2 mM MgSO$_4$, 1.25 mM KH$_2$PO$_4$, 2 mM CaCl$_2$, 10 mM glucose, 10 mM HEPES and 10 nM TMRE (T669, Thermo)]. After incubation for 20 min at 37 °C in the dark, the staining solution was discarded and cells were resuspended in PBS. For H2DCFDA staining, cells were washed three times with PBS, stained with 50 μM H2DCFDA (D399, Thermo) in culture media for 30 min at 37 °C in the dark, washed, trypsinized and resuspended in PBS. For MitoSOX Red staining, cells were washed three times with PBS, trypsinized and resuspended in culture media containing 5 μM MitoSOX Red (M36008, Thermo) dissolved in DMSO. After staining for 10 min at 37 °C in the dark, cells were washed and resuspended in PBS; centrifugation steps were performed in 15 ml conical tubes at $600 \times g$. Propidium iodide staining, with or without prior overnight exposure to 0.25 μM rotenone (R8875, Sigma), was performed as described in [25]. After appropriate staining, cell data acquisition was performed by FACSCalibur or BD Accuri C6 flow cytometers (Becton Dickinson, Franklin Lakes NJ). FlowJo vX. 0.7 (FlowJo LLC, Ashland OR) was used for analysis. Autofluorescent cells were excluded by red (H2DCFDA) or green (TMRE and MitoSOX Red) signal following definition of forward Scattering (FSC) and Side Scattering (SSC) parameters, used to identify cells and exclude debris. Flow cytometry raw data were deposited in flowrepository under the accessions: FR-FCM-ZY2Q for TMRE, FR-FCM-ZY2N for H2DCFDA; FR-FCM-ZY2X for MitoSOX and FR-FCM-ZY2P for Propidium iodide.

2.7. Evaluation of NAD(P)H and FAD autofluorescence in live cells

In vivo FAD and NAD(P)H signals were measured according to [26] and recorded by setting the Leica TCSSP5 MP "Laser (MP, MP) (Power)" at "1747.00 W (720 nm)%", using a HC PL IRAPO 40x water objective to avoid geometric aberrations. According to the protocol [26], regions of interest (ROI) were selected on the basis of high mitochondrial density and fluorescence measured by LAS-Lite 4.2 program (Leica Microsystems CMS GmbH, Mannheim, Germany); numerical analysis was performed by Excel software (Microsoft, Redmond, WA).

2.8. Western blotting analysis

Unless otherwise stated, proteins were extracted from confluent cells and analyzed by western blotting as previously described [19]. The Page ruler (26616, Thermo) was used as protein ladder; β-tubulin was used as internal loading control. Membrane pictures were taken by a ChemiDoc XRS+ System (Bio-Rad, Hercules CA), bands densities analyzed with Image Lab Software (Bio-Rad) and numerical analysis performed by Excel software (Microsoft). Antibodies used are listed in Appendix A, Supplemental Table 1.
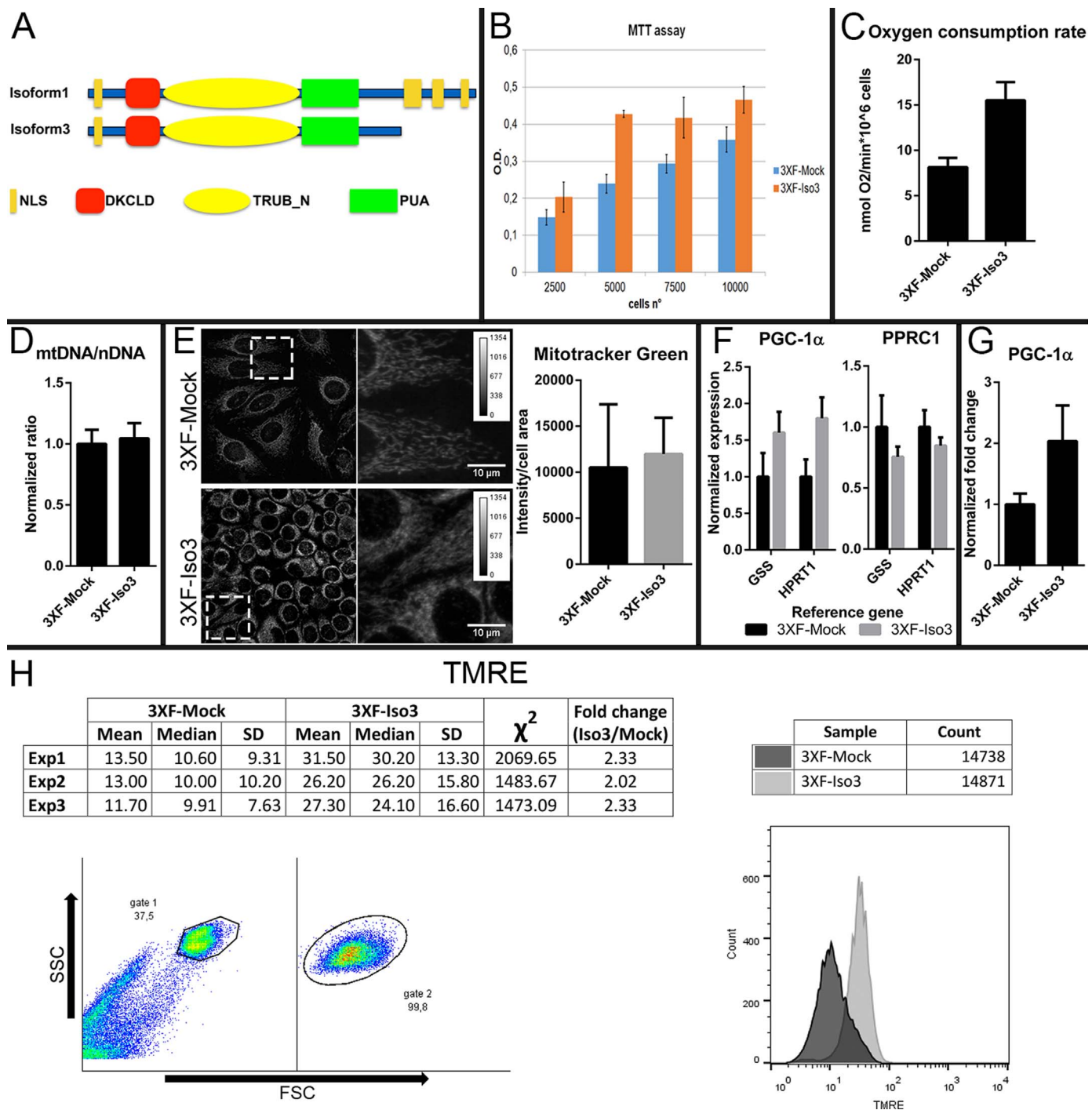
A

Isoform1

Isoform3

NLS   DKCLD   TRUB_N   PUA

B MTT assay

O.D.

2500   5000   7500   10000
cells n°

3XF-Mock
3XF-Iso3

C Oxygen consumption rate

nmol O2/min*10^6 cells

3XF-Mock   3XF-Iso3

D mtDNA/nDNA

Normalized ratio

3XF-Mock   3XF-Iso3

E

3XF-Mock

3XF-Iso3

10 µm

Mitotracker Green

Intensity/cell area

3XF-Mock   3XF-Iso3

F PGC-1α   PPRC1

Normalized expression

GSS   HPRT1   GSS   HPRT1
Reference gene

3XF-Mock   3XF-Iso3

G PGC-1α

Normalized fold change

3XF-Mock   3XF-Iso3

H TMRE

	3XF-Mock			3XF-Iso3			χ^2	Fold change (Iso3/Mock)
	Mean	Median	SD	Mean	Median	SD		
Exp1	13.50	10.60	9.31	31.50	30.20	13.30	2069.65	2.33
Exp2	13.00	10.00	10.20	26.20	26.20	15.80	1483.67	2.02
Exp3	11.70	9.91	7.63	27.30	24.10	16.60	1473.09	2.33

Sample	Count
3XF-Mock	14738
3XF-Iso3	14871

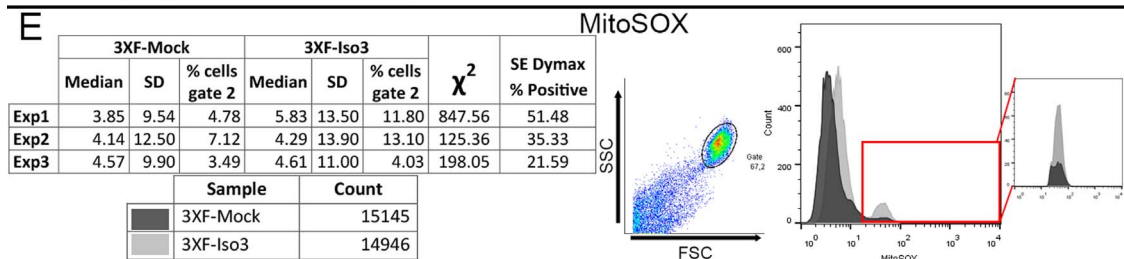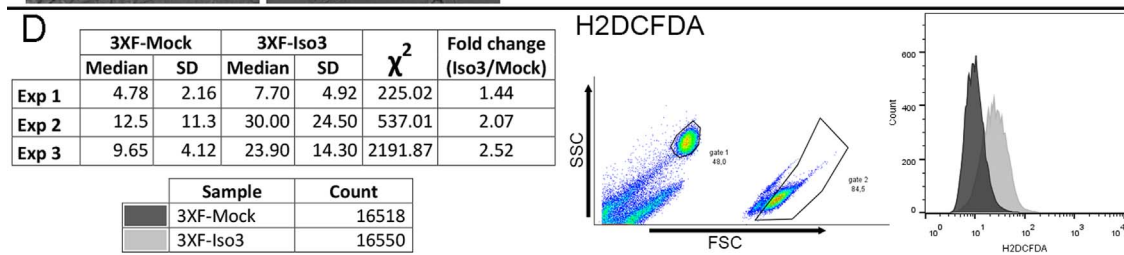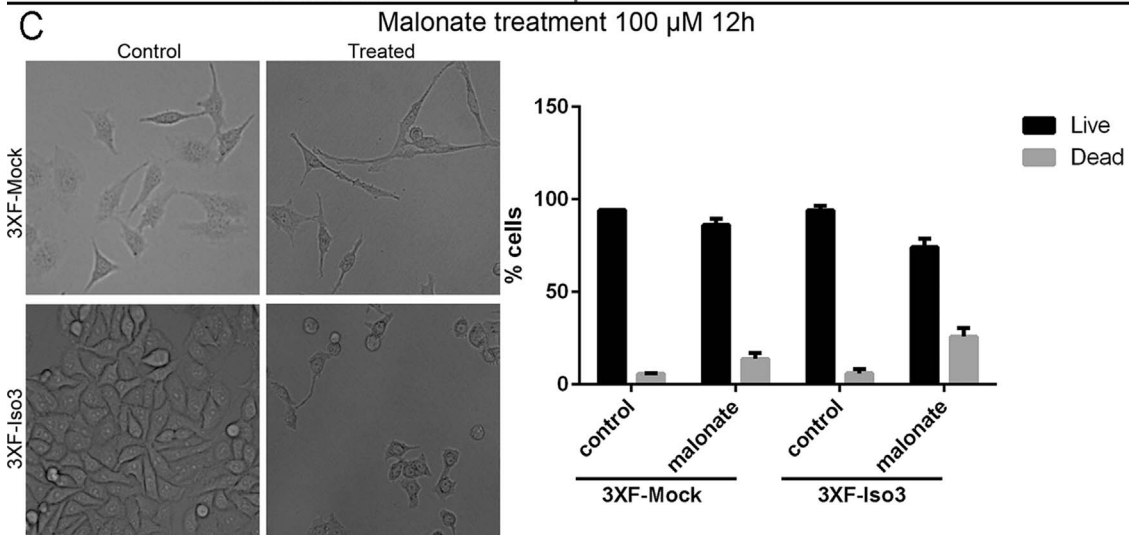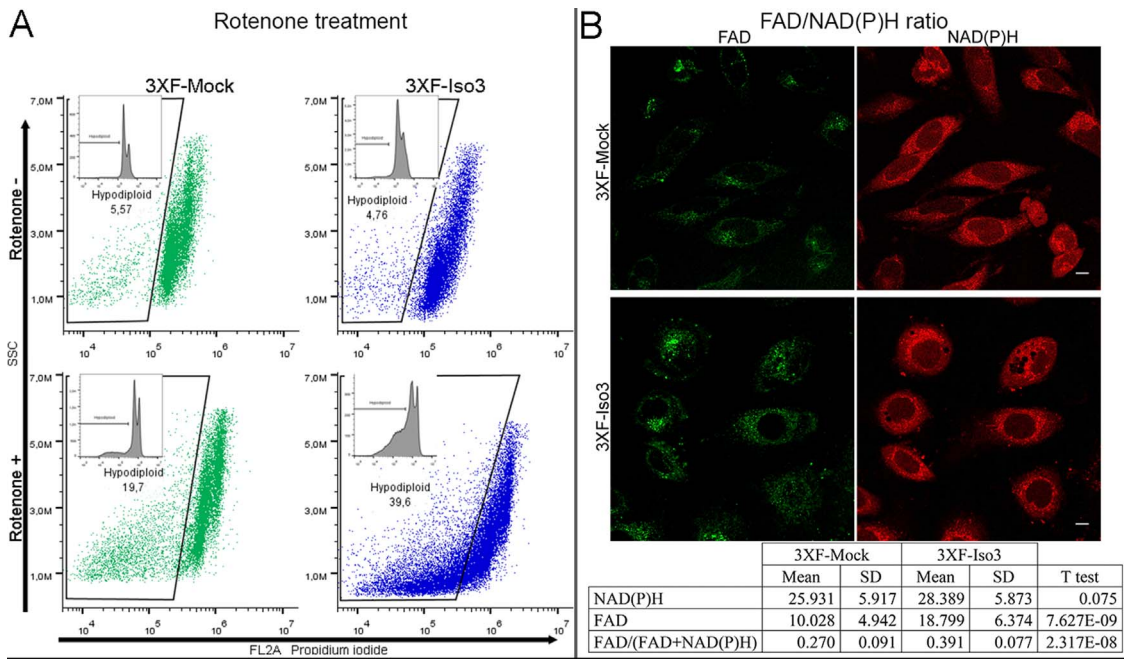gate 1 37,5

gate 2 99,8

SSC

FSC

Count

TMRE

Fig. 1. Overexpression of dyskerin Isoform3 boosts respiratory rate and mitochondrial membrane potential. **(A)** Schematic organization of full-length dyskerin (Isoform1) and dyskerin Isoform 3, lacking the C-terminal NLS. Colored boxes indicate structural domains: DKCLD, associated N-terminal domain of dyskerin-like proteins of unknown function; TRUB_N, pseudouridine synthase catalytic domain; PUA, pseudouridine synthase and archaeosine transglycosylase RNA binding domain; orange boxes, lysine-arginine rich NLS sequences. **(B)** 3XF-Iso3 and control cells ($2.5 * 10^3$–$1 * 10^4$) were seeded in triplicate, incubated overnight to allow attachment and the following day subjected to MTT assay to measure cell proliferation and metabolic activities. The amount of precipitated formazan was quantified by absorbance and expressed as optical density. **(C)** Oxygen consumption rate of 3XF-Iso3 and control cells was measured by Clark's electrode. Note that respiration, expressed as nmol O_2/min $* 10^6$ cells, was nearly doubled in 3XF-Iso3 cells. **(D)** Mitochondrial /nuclear DNA content was quantified by qPCR; the mitochondrial/nuclear DNA ratio is reported. In this experiment, the 16S rRNA coding region was amplified and normalized with respect to the TSH receptor (TSHR) single-copy nuclear gene. **(E)** On the left: LUT quantitative analysis of confocal images of 3XF-Iso3 and 3XF-Mock viable cells, captured under the same conditions, upon staining with MitoTracker Green (in gray), which is insensitive to mitochondrial ΔΨ and allows a direct visualization of the mitochondrial network. Sum of total confocal planes is shown; magnification: 40×; scale bars: 10 µm. The white-dashed squares are enlarged in the insets. On the right: to estimate the mitochondrial mass, the intensity of the MitoTracker Green fluorescent signal was calculated from the same confocal images; values obtained from the sum of total planes were normalized in respect to cell areas and expressed as Intensity/cell area ratio by ImageJ tools. Data derived from the analysis of n = 90 cells. **(F)** qRT-PCR analysis of PGC-1α and PPRC1 expression in 3XF-Iso3 and 3XF-Mock quiescent cells; GSS and HPRT1 were used as normalizing reference genes. **(G)** Histogram representative of PGC-1α expression in 3XF-Iso3 and 3XF-Mock quiescent cells, as derived from western blotting densitometric quantification normalized with respect to β-tubulin (original data in Supplemental Fig. 1A). **(H)** Mitochondrial ΔΨ determined by flow cytometry analysis of TMRE stained cells. The TMRE dye permeates and is sequestered in active mitochondria, so that the amount of sequestered dye is directly dependent on mitochondrial ΔΨ. On the left, data derived from three different experiments; on the right, one representative experiment. Gate 1 represents the population identified as "cells"; gate 2 the "stained" population. In the right histogram, fluorescence intensity is plotted vs. cells count. All experiments were performed in triplicate; in **B–D, F–H** data are expressed as the mean ± SD.

A   Rotenone treatment

B   FAD/NAD(P)H ratio

	3XF-Mock		3XF-Iso3		
	Mean	SD	Mean	SD	T test
NAD(P)H	25.931	5.917	28.389	5.873	0.075
FAD	10.028	4.942	18.799	6.374	7.627E-09
FAD/(FAD+NAD(P)H)	0.270	0.091	0.391	0.077	2.317E-08

C   Malonate treatment 100 µM 12h

D

	3XF-Mock		3XF-Iso3		χ^2	Fold change (Iso3/Mock)
	Median	SD	Median	SD		
Exp 1	4.78	2.16	7.70	4.92	225.02	1.44
Exp 2	12.5	11.3	30.00	24.50	537.01	2.07
Exp 3	9.65	4.12	23.90	14.30	2191.87	2.52

Sample	Count
3XF-Mock	16518
3XF-Iso3	16550

H2DCFDA

E

MitoSOX

	3XF-Mock			3XF-Iso3			χ^2	SE Dymax % Positive
	Median	SD	% cells gate 2	Median	SD	% cells gate 2		
Exp1	3.85	9.54	4.78	5.83	13.50	11.80	847.56	51.48
Exp2	4.14	12.50	7.12	4.29	13.90	13.10	125.36	35.33
Exp3	4.57	9.90	3.49	4.61	11.00	4.03	198.05	21.59

Sample	Count
3XF-Mock	15145
3XF-Iso3	14946

(caption on next page)

Fig. 2. Redox state and ROS induction in Isoform 3 over-expressing cells. (A) Cells were stained with propidium iodide and analyzed by flow cytometry in the absence (−) or following overnight treatment with 0.25 μM rotenone (+). Percentages refer to the total number of examined cells, while plots compare an equal number (10.000) of 3XF-Iso3 and control cells. Note that the fraction of hypodiploid cells does not increase in untreated 3XF-Iso3 cells, indicating that Iso3 overexpression per se does not affect the healthy state of cell population; in contrast, this fraction significantly increases in the 3XF-Iso3 cell population upon rotenone treatment. **(B)** Cellular redox status analyzed by live multiconfocal microscopy following near-infra red excitation. Upper panel shows confocal micrographs of FAD (green) and NAD(P)H (red) autofluorescence signals; lower table reports statistical analysis of fluorescence signals from at least 50 analyzed ROI, selected on the basis of their high mitochondrial content; values are expressed as gray scale units. Scale bars: 10 μm. **(C)** 3XF-Iso3 cells are more sensitive to malonate treatment compared to controls. In both cases, the treatment induces a marked change in cells (on the left). **(D–E)** Total ROS and mitochondrial superoxide levels were measured upon H2DCFDA or MitoSOX Red staining and flow cytometry analysis. Right inset (red rectangle) in D highlights the increase of the superoxide high-producer cell fraction present in 3XF-Iso3 population, identified as "% cells gate 2" in the exp 1 reported in the enclosed table.

2.9. Statistical analysis

Experiments were performed in biological triplicates; the Mann-Whitney test for variance analysis was applied. A difference of p < 0.05 was considered statistically significant.

3. Results

3.1. Dyskerin isoform 3 boosts energy metabolism

In our previous study, we showed that a truncated dyskerin variant, named Isoform 3 (hereafter called Iso3) retained all dyskerin functional domains, with the exception of the C-terminal bipartite nuclear localization signal (NLS) (see Fig. 1A), and displayed a peculiar subcellular localization, being predominantly cytoplasmic [19]. To gain more information about its impact on cell metabolism, we took advantage of previously obtained stably-transfected HeLa clones (hereafter called 3XF-Iso3) that overexpress this Flag-tagged isoform under the control of the CMV promoter [19]. First, we performed a (MTT) reduction assay, commonly used for assessing cell proliferation and metabolic activities. As showed in Fig. 1B, the reduction of tetrazole to formazan salt markedly increased in 3XF-Iso3 with respect to control cells (carrying the p3XFLAG-CMV-10 empty vector; hereafter called 3XF-Mock). Since MTT reduction is mainly dependent on mitochondrial reductases [22], we next evaluated the total oxygen consumption rate and found that it was raised significantly in 3XF-Iso3 cells, indicating that cellular respiration was upregulated (Fig. 1C). Given that mitochondrial activity generally correlates directly with mitochondrial number/mass, we next calculated the mitochondrial/nuclear DNA ratio by qPCR. As shown in Fig. 1D, this value remained substantially unchanged compared to control cells. To reaffirm this point, we stained cells with MitoTracker green, which is insensitive to mitochondrial membrane potential (ΔΨ) and allows the direct visualization of the mitochondrial network. In these experiments, confocal images of 3XF-Iso3 and 3XF-Mock cells were acquired with the same parameters and subjected to LUT quantitative analysis by ImageJ tools, to precisely quantify the mitochondrial mass. To take into consideration the distinct morphologies of 3XF-Iso3/ 3XF-Mock cells [19], the intensity of the fluorescent signal was normalized per cell area. Consistent with previous observation, this analysis indicated that the mitochondrial mass does not increase in 3XF-Iso3 cells (Fig. 1E). We then used reverse qRT-PCR to check the expression of members of the PGC-1 family of positive regulators of cellular respiration. Transcription of peroxisome proliferator-activated receptor gamma coactivator-1alpha (PGC-1α) was found modestly induced (≈ 1.8 fold) in 3XF-Iso3 quiescent cells, while that of peroxisome proliferator-activated receptor gamma co-activator-related 1 (PPRC1) slightly decreased (Fig. 1F). PGC-1α expression was further checked by western blotting analysis (Fig. 1G; Supplemental Fig. 1A). PGC-1α is a master regulator of mitochondrial activity whose induction can be due to different physiological context and stimuli; it can exert a positive impact on cellular respiration by either increasing the number of mitochondria in cells or by improving the respiratory capacity of individual mitochondria, remodeling their composition (reviewed in [27]). Given that direct measurements showed that the mitochondrial mass was unaffected by Iso3 over-expression (Fig. 1D, E), we presumed that PGC-1α induction in 3XF-Iso3 quiescent cells might contribute to

mitochondrial remodeling. To note, PGC-1α also promotes peroxisomal biogenesis and remodeling and stimulates the increase in content of ROS-detoxifying enzymes, thereby improving cell survival during conditions of oxidative stress [27]. Instead, lowered PPRC1 expression has been associated with elevated basal metabolic rate and increased energy expenditure [28]. Altogether, these results lead to focus our attention on mitochondrial activity, prompting us to measure the mitochondrial membrane potential. When TMRE-stained cells were analyzed by Flow cytometry, a significant increase of mitochondrial membrane polarization was observed in 3XF-Iso3 cells (Fig. 1H). Considering that mitochondrial ΔΨ is directly linked to the proton gradient generated through the electron transport chain (ETC), and is a direct indicator of the efficiency of coupling between respiration and ATP production, these results converged to indicate that Iso3 overexpression stimulates respiration efficiency and energy metabolism.

3.2. Dyskerin Iso3 modulates global redox ratio and ROS level

To further investigate the relationship between respiratory efficiency and increased growth rate, we treated cells with rotenone, which blocks the ETC by specifically inhibiting complex I [29], and analyzed them by FACS after propidium iodide staining. As shown in Fig. 2A, 3XF-Iso3 cells were more sensitive to rotenone-induced cytotoxicity compared to controls, suggesting that their enhanced growth rate is primarily dependent on a higher respiratory efficiency. Next, we determined the cellular global redox level, which is regulated by the equilibrium between the oxidized and reduced forms of NADH/NAD+, NADPH/NADP+ [altogether NAD(P)H/NAD(P)+] and FADH2/FAD, which are the main cellular redox cofactors. NAD(P)H and FAD are the only two ETC cofactors to be intrinsically fluorescent, with their fluorescence depending on binding to metabolic enzymes. In fact, NAD(P)H quantum yield increases, whereas FAD quantum yield decreases, when they are bound to proteins [30–32]. To precisely determine the redox ratio, we utilized multiphoton confocal laser microscopy following near-infra red excitation, that allows for the evaluation of the NAD(P)H and FAD autofluorescence in live cells with high resolution, while avoiding any staining or cell manipulation [26]. While NAD(P)H fluorescence was found substantially unchanged in 3XF-Iso3 cells, FAD fluorescence increased significantly with respect to the control (Fig. 2B). This resulted in a significant rise in the redox ratio [expressed as FAD/(FAD + NAD(P)H)], and suggested a more active reduction of ubiquinone to ubiquinol by complex II, the reaction coupled with FADH2 oxidation. This view is further supported by the observation that treatment with dimethyl malonate, a permeable precursor of the SDH inhibitor malonate, reduced more severely the vitality of 3XF-Iso3 compared to controls, as observed by Trypan Blue viable cell count (Fig. 2C).

Next, we checked total ROS and mitochondrial superoxide levels by Flow Cytometry analysis of cells stained with H2DCFDA or MitoSOX Red, respectively. As shown in Fig. 2D–E, both levels increased upon Iso3 over-expression. Interestingly, Flow Cytometry of MitoSOX stained cells revealed that 3XF-Iso3 and control cells were both composed of two subpopulations, specifically characterized by low or high mitochondrial superoxide levels (note the double peaks in Fig. 2E). However, the fraction of cells that incorporate higher levels of MitoSOX increases markedly in 3XF-Iso3 cells (by SE Dymax calculation, more
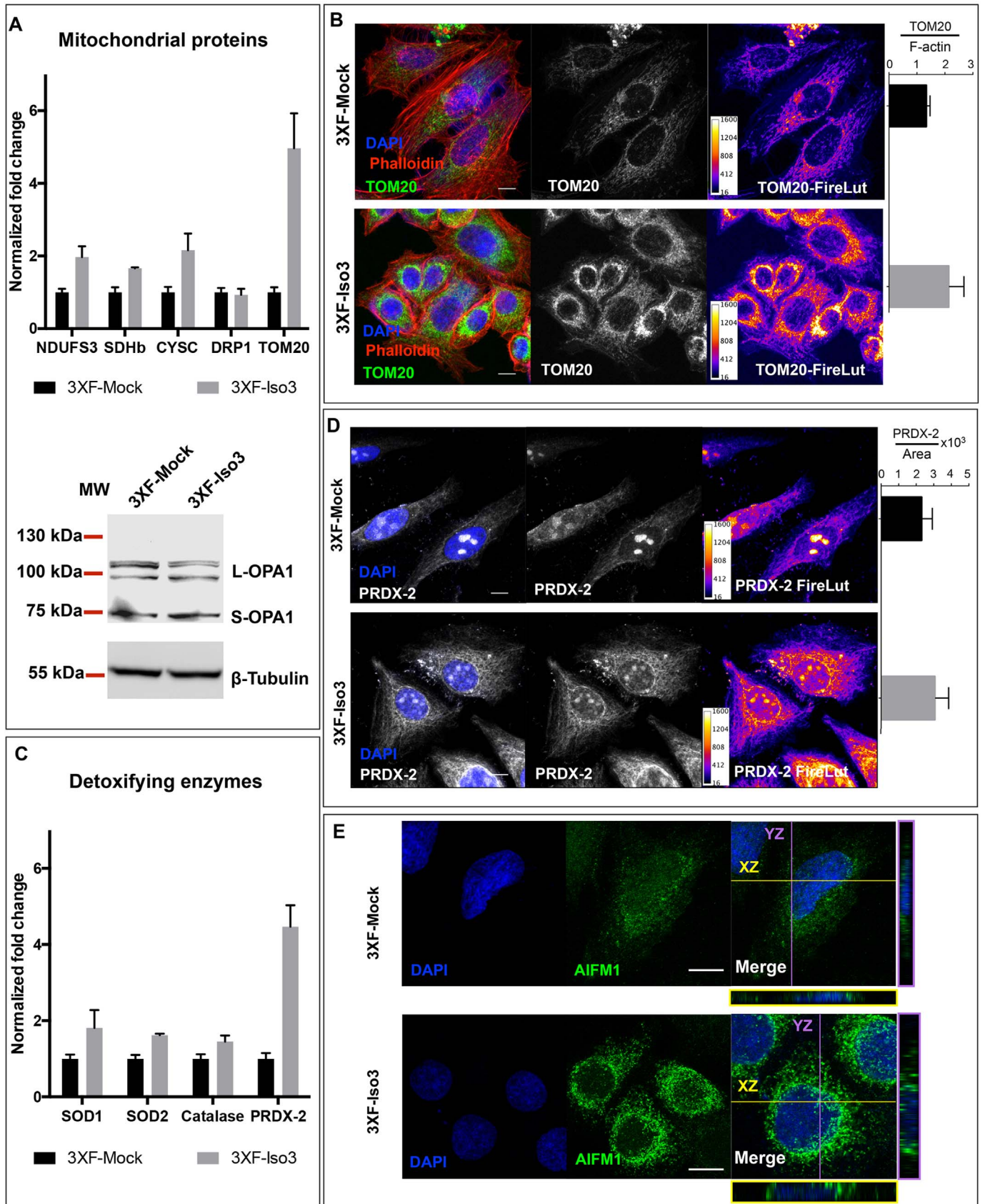
(caption on next page)

Fig. 3. Enhanced expression of mitochondrial proteins and detoxification enzymes contribute to the healthy state of Iso3 over-expressing cells. On the top are histograms representative of expression levels of ETC components and key mitochondrial proteins. Data derived from western blotting densitometric quantification, normalized with respect to β-tubulin (original data in Supplemental Fig. 1B); Note that NDUFS3 (Complex I), SDHb (complex II), CYSC (Complex III) levels all increased in 3XF-Iso3 cells; instead, expression of DRP1, which promotes mitochondrial fission, and of OPA1, a pro-fusion protein that produces long (L-OPA1) and short (S-OPA1) isoforms (bottom), remained substantially unvaried. Expression of TOM20, a component of the outer mitochondrial membrane, was significantly up-regulated in 3XF-Iso3 cells. (B) LUT quantitative analysis of confocal images, captured under the same conditions, depicting TOM20 expression in 3XF-Iso3 and 3XF-Mock cells. The anti-TOM20 antibody (green/gray) stains the mitochondrial network; Phalloidin (red) marks the actin cytoskeleton; DAPI (blue) counterstains the nuclei. Images are at 63× magnification; scale bars: 10 μm; the sum of total confocal planes is shown. On the right: intensity signal values obtained from the sum of total planes were normalized with respect to F-actin signal and expressed as TOM20 intensity/actin intensity ratio by ImageJ tools. Data derived from the analysis of n = 50 cells. (C) Histograms representative of expression levels of a panel of detoxifying enzymes. Data derived from western blotting densitometric quantification, normalized with respect to β-tubulin (original data in Supplemental Fig. 1C). (D) LUT quantitative analysis of confocal images, captured under the same conditions, of 3XF-Iso3 and 3XF-Mock cells stained with anti-PRDX-2 (gray); nuclei are counterstained by DAPI (blue). Sum of total planes is shown; magnification is at 63×; scale bars: 10 μm. On the right: intensity signal values obtained from the sum of total planes were normalized with respect to cell areas and expressed as Intensity/cell area ratio by ImageJ tools. Data derived from the analysis of n = 50 cells. (E) Confocal images of 3XF-Iso3 and 3XF-Mock cells upon staining with the anti-AIFM1 antibody (green); nuclei are counterstained by DAPI (blue). On the left, maximum projection of z-stack confocal planes; on the right, maximum projection of z-stack, flanked by orthogonal views. Scale bars: 10 μm. In A, C, blotting were performed in triplicate, and data expressed as the mean ± SD.

than 36% of 3XF-Iso3 cells resulted positive with respect to the control), with the superoxide high-producer population consisting of about three times the number of cells with respect to that of the control (see inset in Fig. 2E and compare "% cells gate 2"). Since increased mitochondrial function and ROS generation correlate with metabolic rate [33], this finding suggests that Iso3 can promote an endogenous metabolic re-wiring resulting at a higher respiratory rate.

3.3. Dyskerin Iso3 induces a ROS adaptive response

To check whether the higher respiratory rate displayed by 3XF-Iso3 cells correlated with overexpression of OXPHOS components, we followed the expression of key ETC enzymes: the NADH-coenzyme Q reductase (NDUFS3; Complex I), the succinate dehydrogenase subunit b (SDHb; Complex II), and the monomeric cytochrome c (CYSC; Complex III). Indeed, all these enzymes showed increased levels in 3XF-Iso3 cells (Fig. 3A; Supplemental Fig. 1B), supporting the notion that ETC activity was improved. We then checked the expression of key regulators of the morphology of the mitochondrial network, which depends on the balance between mitochondrial fission and fusion, and ultimately reflects mitochondrial functionality (reviewed by [34]). First, we followed the expression of DRP1, a dynamin-related protein that promotes mitochondrial fission [35], and found its level substantially unchanged in 3XF-Iso3 cells (Fig. 3A). Next, we examined OPA1, a pro-fusion protein present in multiple isoforms [defined as long (L-OPA1) or short (S-OPA1)] produced by both alternative splicing and proteolytic processing; a disproportionate accumulation of S-OPA1 forms is known to correlate with mitochondrial fragmentation and loss of mitochondrial ΔΨ [36,37]. Consistent with previous results, no excessive accumulation of S-OPA1 forms was observed in 3XF-Iso3 cells (Fig. 3A), although the longest L-OPA1 isoform appeared slightly underproduced (Fig. 3A).

Next, we focused on TOM20, a key marker of the outer mitochondrial membrane that acts as a receptor for the import of mitochondrial pre-proteins (reviewed by [38]). Intriguingly, expression of this protein was found to be significantly up-regulated in 3XF-Iso3 cells, as shown by both western blotting and LUT quantitative analyses of confocal images (Fig. 3A, B). Since TOM20 upregulation can have beneficial effects on cell growth [39], it is plausible that this trait may contribute to improving mitochondrial functionality. Note that, although TOM20 expression is usually taken as a marker of increased mitochondrial biogenesis, it is known that it has additional localization on vesicles that detach from mitochondria and transport selected cargo to peroxisomes [40] and lysosomes [41].

We thus wondered whether 3XF-Iso3 cells could counteract ROS-induced deleterious effects by improving their anti-oxidant defenses. The expression of key detoxifying enzymes, such as superoxide dismutases1 (SOD1; cytoplasmic) and 2 (SOD2; mitochondrial), catalase (peroxisomal), and redox-regulatory protein peroxiredoxin 2 (PRDX-2; cytoplasmic) was then measured by western blotting. Levels of these enzymes all increased in 3XF-Iso3 cells (Fig. 3C; Supplemental Fig. 1C); however, catalase, SOD1 and SOD2 were only modestly enhanced,

while PRDX-2 was dramatically upregulated, suggesting a specific role in the ROS tolerance of 3XF-Iso3 cells. Enhanced PRDX-2 expression was confirmed by LUT quantitative analysis of confocal images (Fig. 3D). Intriguingly, analysis of PRDX-2 intracellular distribution revealed that this protein concentrates specifically in the nucleoli in both 3XF-Iso3 and control cells (Fig. 3D). To our knowledge, this is the first report of PRDX-2 nucleolar localization. Robust expression of PRDX-2 protects cells against oxidative stress [42,43]; moreover, PRDX-2 nuclear translocation is reported to safeguard cancer cells from DNA-damaging agents [44]. We also noted that in the cytoplasm of control cells PRDX-2 assumed a mostly vesicular pattern, while in Iso3 cells it displayed a more filamentous arrangement (Fig. 3D), typical of the protein hyperoxidation state [45]. PRDX-2 hyperoxidation leads to its temporary inactivation, a state that has been linked to the acquisition of chaperone function and of a regulatory role in redox-dependent signaling (reviewed by [46,47]). In its reversible inactive state, PRDX-2 can in fact act as a "floodgate" [47], permitting hydrogen peroxide to accumulate and act as a diffusible secondary messenger in redox-dependent signaling [47,48]. Lastly, to check whether ROS over-production could induce damage to nuclear DNA, we followed the subcellular localization of the apoptosis-inducing factor mitochondrion-associated 1 (AIFM1), a NADH oxidoreductase flavoprotein that resides in mitochondrial intermembrane space but, in response to apoptotic stimuli, translocates to the nucleus and promotes apoptosis [49]. As shown in Fig. 3E, the absence of AIFM1 nuclear translocation further confirmed the healthy state of 3XF-Iso3 cells, in line with previous results of FACS analysis. Collectively, these data support the view that 3XF-Iso3 cells acquired a tolerance to increased levels of endogenous ROS.

4. Discussion

We showed that Iso3, a truncated dyskerin splice-variant, exhibits new uncanonical functions, having the ability to promote a metabolic shift that enhances the respiratory rate without significantly altering the mitochondrial volume. Since mitochondria represent the main source of ROS in many cell types (reviewed by [50]), it is not surprising that the observed respiratory boost is accompanied by augmented ROS generation. Specific enzymes, such as those of the NADPH oxidase (NOX) family, can contribute to increased ROS formation; however, if this was true, in 3XF-Iso3 cells the NAD(P)H/NAD(P)+ ratio would have shifted towards its oxidized form. Conversely, this ratio was unchanged, while the FAD/(FAD + NAD(P)H) ratio increased. In addition, the findings that rotenone and dimethyl malonate treatments have a stronger effect on the survival of 3XF-Iso3 cells demonstrate their higher dependence on OXPHOS compared to controls. Worth noting are the findings by Thyagarajan et al., that Iso3 is upregulated by incubation with hydrolysis products generated by lipoprotein lipase [21]. Since fatty acid β-oxidation occurs in both mitochondria and peroxisomes, the increased level of catalase observed in 3XF-Iso3 cells fits well with the possibility that Iso3 might fuel OXPHOS through this

route.

Although further experiments need to be performed to define the specific molecular pathways stimulated by Iso3 overexpression, it is reasonable to suppose that the protein could have a general impact on snoRNA-mediated processes, including pseudouridylation, thereby concomitantly regulating multiple processes connecting energy metabolism with cell homeostasis. Several considerations support this view: first, snoRNAs are assuming expanding roles in the regulation of cell homeostasis [51]; second, the mammalian transcriptome is known to be pseudouridylated in a specific manner according to diverse metabolic conditions [52]; third, Drosophila dyskerin is deeply implicated in the regulation of cell homeostasis in vivo [53–55].

We also demonstrated that the boost in ROS production is efficiently counterbalanced by antioxidant defenses, allowing 3XF-Iso3 cells to acquire a ROS adaptive tolerance. Note that this finding suggests novel mechanisms by which *DKC1* overexpression might contribute to cancer aggressiveness, particularly in cancer cell types known to synthesize ATP mainly through mitochondrial respiration (reviewed by [56]). Mitochondrial ROS have been implicated in mitochondria-to-nucleus signaling, regulating the expression of detoxifying enzymes, with hydrogen peroxide appearing to be the main ROS with such signaling properties. Peroxidases have a high affinity for hydrogen peroxide and act as localized sensors of this molecule in specialized compartments [47]. Indeed, the NADPH-dependent cytosolic PRDX-2 enzyme is likely to play a key role in activating the ROS protective response of 3XF-Iso3 cells, and possibly in stimulating their proliferative rate. In fact, in many types of cancer cells characterized by high level of ROS production, PRDX-2 up-regulation serves as a mechanism of defense against oxidative damage, assuring survival and proliferation [57,58]; in addition, PRDX-2 has been identified as the molecular link that propagates the ROS beneficial signal in the mitohormetic pathway [59].

Taken together, the data reported here reveal a new moonlight function for the *DKC1* gene, whose more abundant protein isoform is restricted to the nuclei, where it is enriched in the nucleoli and the Cajal bodies (reviewed by [5]). Several proteins thought to have specific nuclear functions have subsequently been found to have an additional localization in the cytoplasm, or more specifically in the mitochondria, and play distinct roles in their diverse subcellular locations (reviewed by [60]). The most striking example is that of telomerase reverse transcriptase (TERT), whose mitochondrial localization improves respiration and protects cells from oxidative stress and apoptosis (reviewed by [61]). Considering that dyskerin participates with TERT in the formation of the nuclear telomerase complex, the ability of its truncated variant to enhance mitochondrial functionality further reinforces the functional relationship between telomerase and mitochondrial status. It will be interesting to see whether, owing to its peculiar cytoplasmic localization, Iso3 can transduce a nucleus-mitochondria signal, or interact with TERT in the cytosol, or even in mitochondria.

Acknowledgements

Conflict of interest

Nothing to claim.

Appendix A. Supplementary material

Supplementary data associated with this article can be found in the online version at http://dx.doi.org/10.1016/j.redox.2017.11.003.

References

[1] N.S. Heiss, S.W. Knight, T.J. Vulliamy, S.M. Klauck, S. Wiemann, P.J. Mason, A. Poustka, I. Dokal, X-linked dyskeratosis congenita is caused by mutations in a highly conserved gene with putative nucleolar functions, Nat. Genet. 19 (1998) 32–38, http://dx.doi.org/10.1038/ng0598-32.

[2] S.B. Cohen, M.E. Graham, G.O. Lovrecz, N. Bache, P.J. Robinson, R.R. Reddel, Protein composition of catalytically active human telomerase from immortal cells, Science 315 (2007) 1850–1853, http://dx.doi.org/10.1126/science.1138596.

[3] P.J. Mason, M. Bessler, The genetics of dyskeratosis congenita, Cancer Genet. 204 (2001) 635–645, http://dx.doi.org/10.1016/j.cancergen.2011.11.002.

[4] I. Dokal, Dyskeratosis congenita, Hematol. Am. Soc. Hematol. Educ. Prog. (2011) 480–486, http://dx.doi.org/10.1182/asheducation-2011.1.

[5] A. Angrisani, R. Vicidomini, M. Turano, M. Furia, Human dyskerin: beyond telomeres, Biol. Chem. 395 (2014) 593–610, http://dx.doi.org/10.1515/hsz-2013-0287.

[6] I. Dokal, T. Vulliamy, P. Mason, M. Bessler, Clinical utility gene card for: dyskeratosis congenita – update 2015, Eur. J. Hum. Genet. 23 (2015) 4, http://dx.doi.org/10.1038/ejhg.2014.170.

[7] M.E. Schaner, D.T. Ross, G. Ciaravino, T. Sorlie, O. Troyanskaya, M. Diehn, Y.C. Wang, G.E. Duran, T.L. Sikic, S. Caldeira, H. Skomedal, I.P. Tu, T. Hernandez-Boussard, S.W. Johnson, P.J. O'Dwyer, M.J. Fero, G.B. Kristensen, A.L. Borresen-Dale, T. Hastie, R. Tibshirani, M. van de Rijn, N.N. Teng, T.A. Longacre, D. Botstein, P.O. Brown, B.I. Sikic, Gene expression patterns in ovarian carcinomas, Mol. Biol. Cell 14 (2003) 4376–4386, http://dx.doi.org/10.1091/mbc.E03-05-0279.

[8] S.L. McDonald, H.D. Edington, J.M. Kirkwood, D. Becker, Expression analysis of genes identified by molecular profiling of VGP melanomas and MGP melanoma-positive lymph nodes, Cancer Biol. Ther. 3 (2004) 110–120.

[9] L. Montanaro, M. Brigotti, J. Clohessy, S. Barbieri, C. Ceccarelli, D. Santini, M. Taffurelli, M. Calienni, J. Teruya-Feldstein, D. Trerè, P.P. Pandolfi, M. Derenzini, Dyskerin expression influences the level of ribosomal RNA pseudouridylation and telomerase RNA component in human breast cancer, J. Pathol. 210 (2006) 10–18.

[10] R. Piva, E. Pellegrino, M. Mattioli, L. Agnelli, L. Lombardi, F. Boccalatte, G. Costa, B.A. Ruggeri, M. Cheng, R. Chiarle, G. Palestro, A. Neri, G. Inghirami, Functional validation of the anaplastic lymphoma kinase signature identifies CEBPB and BCL2A1 as critical target genes, J. Clin. Invest. 116 (2006) 3171–3182, http://dx.doi.org/10.1172/JCI29401.

[11] F. Westermann, K.O. Henrich, J.S. Wei, W. Lutz, M. Fischer, R. König, R. Wiedemeyer, V. Ehemann, B. Brors, K. Ernestus, I. Leuschner, A. Benner, J. Khan, M. Schwab, High Skp2 expression characterizes high-risk neuroblastomas independent of MYCN status, Clin. Cancer Res. 13 (2007) 4695–4703, http://dx.doi.org/10.1158/1078-0432.CCR-06-2818.

[12] L. Montanaro, M. Calienni, C. Ceccarelli, D. Santini, M. Taffurelli, S. Pileri, D. Treré, M. Derenzini, Relationship between dyskerin expression and telomerase activity in human breast cancer, Cell. Oncol. 30 (2008) 483–490.

[13] M. Turano, A. Angrisani, M. De Rosa, P. Izzo, M. Furia, Real-time PCR quantification of human DKC1 expression in colorectal cancer, Acta Oncol. 47 (2008) 1598–1599, http://dx.doi.org/10.1080/02841860801898616.

[14] P. Sieron, C. Hader, J. Hatina, R. Engers, A. Wlazlinski, M. Müller, W.A. Schulz, DKC1 overexpression associated with prostate cancer progression, Br. J. Cancer 101 (2009) 1410–1416, http://dx.doi.org/10.1038/sj.bjc.6605299.

[15] A. Witkowska, J. Gumprecht, J. Glogowska-Ligus, G. Wystrychowski, A. Owczarek, M. Stachowicz, A. Bocianowska, E. Nowakowska-Zajdel, U. Mazurek, Expression profile of significant immortalization genes in colon cancer, Int. J. Mol. Med. 25 (2010) 321–329.

[16] B. Liu, J. Zhang, C. Huang, H. Liu, Dyskerin overexpression in human hepatocellular carcinoma is associated with advanced clinical stage and poor patient prognosis, PLoS One 7 (2012) e43147, http://dx.doi.org/10.1371/journal.pone.0043147.

[17] K. von Stedingk, J. Koster, M. Piqueras, R. Noguera, S. Navarro, S. Påhlman, R. Versteeg, I. Ora, D. Gisselsson, D. Lindgren, H. Axelson, snoRNPs regulate telomerase activity in neuroblastoma and are associated with poor prognosis, Transl. Oncol. 6 (2013) 447–457.

[18] T. Sbarrato, E. Horvilleur, T. Pöyry, K. Hill, L.C. Chaplin, R.V. Spriggs, M. Stoneley, L. Wilson, S. Jayne, T. Vulliamy, D. Beck, I. Dokal, M.J. Dyer, A.M. Yeomans, G. Packham, M. Bushell, S.D. Wagner, A.E. Willis, A ribosome-related signature in peripheral blood CLL B cells is linked to reduced survival following treatment, Cell Death Dis. 7 (2016) e2249, http://dx.doi.org/10.1038/cddis.2016.148.

[19] A. Angrisani, M. Turano, L. Paparo, C. Di Mauro, M. Furia, A new human dyskerin isoform with cytoplasmic localization, Biochim. Biophys. Acta 1810 (2011) 1361–1368, http://dx.doi.org/10.1016/j.bbagen.2011.07.012.

[20] M. Turano, A. Angrisani, N. Di Maio, M. Furia, Intron retention: a human DKC1 gene common splicing event, Biochem. Cell Biol. 91 (2013) 506–512, http://dx.doi.org/10.1139/bcb-2013-0047.

[21] N. Thyagarajan, J.D. Marshall, A.T. Pickett, C. Schumacher, Y. Yang, S.L. Christian, R.J. Brown, Transcriptomic analysis of THP-1 macrophages exposed to lipoprotein hydrolysis products generated by lipoprotein lipase, Lipids 52 (2017) 189–205, http://dx.doi.org/10.1007/s11745-017-4238-1.

[22] M.V. Berridge, A.S. Tan, Characterisation of the cellular reduction of 3-(4,5-dimethylthiazol-2-yl)-2,5-diphenyltetrazolium bromide (MTT): subcellular localization, substrate dependence, and involvement of mitochondrial electron transport in MTT reduction, Arch. Biochem. 303 (1993) 474–482.

[23] W.S. Rasband, ImageJ, U. S. National Institutes of Health, Bethesda, Maryland, USA, 1997–2016. ⟨http://imagej.nih.gov/ij/⟩.

[24] A. Untergasser, I. Cutcutache, Y. Koressaar, J. Ye, B.C. Faircloth, M. Remm, S.G. Rozen, Primer3 – new capabilities and interfaces, Nucleic Acids Res. 40 (2012)

e115, http://dx.doi.org/10.1093/nar/gks596.

[25] Z. Darzynkiewicz, G. Juan, DNA content measurement for DNA ploidy and cell cycle analysis (Chapter 7: Unit 7.5), Curr. Protoc. Cytom. (2001), http://dx.doi.org/10.1002/0471142956.cy0705s00.

[26] A.V. Kuznetsov, R. Margreiter, A. Amberger, V. Saks, M. Grimm, Changes in mitochondrial redox state, membrane potential and calcium precede mitochondrial dysfunction in doxorubicin-induced cell death, Biochim. Biophys. Acta 1813 (2011) 1144–1152, http://dx.doi.org/10.1016/j.bbamcr.2011.03.002.

[27] S. Austin, J. St-Pierre, PGC1α and mitochondrial metabolism–emerging concepts and relevance in ageing and neurodegenerative disorders, J. Cell Sci. 125 (2012) 4963–4971, http://dx.doi.org/10.1242/jcs.113662.

[28] N. Zhai, C. Sun, W. Gu, X. He, A. Shan, H. Sun, N. Lu, B. Cui, G. Ning, Resistance to high-fat diet-induced obesity in male heterozygous Pprc1 knockout mice, Endocr. J. 62 (2015) 633–644, http://dx.doi.org/10.1507/endocrj.EJ14-0383.

[29] N. Li, K. Ragheb, G. Lawler, J. Sturgis, B. Rajwa, J.A. Melendez, J.P. Robinson, Mitochondrial complex I inhibitor rotenone induces apoptosis through enhancing mitochondrial reactive oxygen species production, J. Biol. Chem. 278 (2003) 8516–8525, http://dx.doi.org/10.1074/jbc.M210432200.

[30] W.S. Kunz, W. Kunz, Contribution of different enzymes to flavoprotein fluorescence of isolated rat liver mitochondria, Biochim. Biophys. Acta 841 (1985) 237–246.

[31] S. Huang, A.A. Heikal, W.W. Webb, Two-photon fluorescence spectroscopy and microscopy of NAD(P)H and flavoprotein, Biophys. J. 82 (2002) 2811–2825, http://dx.doi.org/10.1016/S0006-3495(02)75621-X.

[32] M.C. Skala, K.M. Riching, A. Gendron-Fitzpatrick, J. Eickhoff, K.W. Eliceiri, J.G. White, N. Ramanujam, In vivo multiphoton microscopy of NADH and FAD redox states, fluorescence lifetimes, and cellular morphology in precancerous epithelia, Proc. Natl. Acad. Sci. USA 104 (2007) 19494–19499, http://dx.doi.org/10.1073/pnas.0708425104.

[33] F. Scialò, A. Sriram, A. Naudí, V. Ayala, M. Jové, R. Pamplona, A. Sanz, Target of rapamycin activation predicts lifespan in fruit flies, Cell Cycle 14 (2015) 2949–2958, http://dx.doi.org/10.1080/15384101.2015.1071745.

[34] T. Wai, T. Langer, Mitochondrial dynamics and metabolic regulation, Trends Endocrinol. Metab. 27 (2016) 105–117, http://dx.doi.org/10.1016/j.tem.2015.12.001.

[35] E. Smirnova, L. Griparic, D.L. Shurland, A.M. van der Bliek, Dynamin-related protein Drp1 is required for mitochondrial division in mammalian cells, Mol. Biol. Cell 12 (2001) 2245–2256.

[36] S. Ehses, I. Raschke, G. Mancuso, S. Geimer, D. Tondera, J.C. Martinou, B. Westermann, E.I. Rugarli, T. Langer, Regulation of OPA1 processing and mitochondrial fusion by m-AAA protease isoenzymes and OMA1, J. Cell Biol. 187 (2009) 1023–1036, http://dx.doi.org/10.1083/jcb.200906084.

[37] B. Head, L. Griparic, M. Amiri, S. Gandre-Babbe, A.M. van der Bliek, Inducible proteolytic inactivation of OPA1 mediated by the OMA1 protease in mammalian cells, J. Cell Biol. 187 (2009) 959–966, http://dx.doi.org/10.1083/jcb.200906083.

[38] C. Schulz, A. Schendzielorz, P. Rehling, Unlocking the presequence import pathway, Trends Cell Biol. 25 (2015) 265–275, http://dx.doi.org/10.1016/j.tcb.2014.12.001.

[39] R. Di Maio, P.J. Barrett, E.K. Hoffman, C.W. Barrett, A. Zharikov, A. Borah, X. Hu, J. McCoy, C.T. Chu, E.A. Burton, T.G. Hastings, J.T. Greenamyre, α-synuclein binds to TOM20 and inhibits mitochondrial protein import in Parkinson's disease (342ra78), Sci. Transl. Med. 8 (2016), http://dx.doi.org/10.1126/scitranslmed.aaf3634.

[40] M. Neuspiel, A.C. Schauss, E. Braschi, R. Zunino, P. Rippstein, R.A. Rachubinski, M.A. Andrade-Navarro, H.M. McBride, Cargo-selected transport from the mitochondria to peroxisomes is mediated by vesicular carriers, Curr. Biol. 18 (2008) 102–108, http://dx.doi.org/10.1016/j.cub.2007.12.038.

[41] V. Soubannier, G.L. McLelland, R. Zunino, E. Braschi, P. Rippstein, E.A. Fon, H.M. McBride, A vesicular transport pathway shuttles cargo from mitochondria to lysosomes, Curr. Biol. 22 (2012) 135–141, http://dx.doi.org/10.1016/j.cub.2011.11.057.

[42] J.C. Moon, Y.S. Hah, W.Y. Kim, B.G. Jung, H.H. Jang, J.R. Lee, S.Y. Kim, Y.M. Lee, M.G. Jeon, C.W. Kim, M.J. Chom, S.Y. Lee, Oxidative stress-dependent structural and functional switching of a human 2-Cys peroxiredoxin isotype II that enhances HeLa cell resistance to H$_2$O$_2$-induced cell death, J. Biol. Chem. 280 (2005) 28775–28784, http://dx.doi.org/10.1074/jbc.M505362200.

[43] L.E. Netto, F. Antunes, The roles of peroxiredoxin and thioredoxin in hydrogen peroxide sensing and in signal transduction, Mol. Cells 39 (2016) 65–71, http://dx.doi.org/10.14348/molcells.2016.2349.

[44] K.W. Lee, D.J. Lee, J.Y. Lee, D.H. Kang, J. Kwon, S.W. Kang, Peroxiredoxin II restrains DNA damage-induced death in cancer cells by positively regulating JNK-dependent DNA repair, J. Biol. Chem. 286 (2011) 8394–8404, http://dx.doi.org/10.1074/jbc.M110.179416.

[45] T.J. Phalen, K. Weirather, P.B. Deming, V. Anathy, A.K. Howe, A. van der Vliet, T.J. Jönsson, L.B. Poole, N.H. Heintz, Oxidation state governs structural transitions in peroxiredoxin II that correlate with cell cycle arrest and recovery, J. Cell Biol. 175 (2006) 779–789, http://dx.doi.org/10.1083/jcb.200606005.

[46] W. Jeong, S.H. Bae, M.B. Toledano, S.G. Rhee, Role of sulfiredoxin as a regulator of peroxiredoxin function and regulation of its expression, Free Radic. Biol. Med. 53 (2012) 447–456, http://dx.doi.org/10.1016/j.freeradbiomed.2012.05.020.

[47] S.G. Rhee, Overview on peroxiredoxin, Mol. Cells 39 (2016) 1–5, http://dx.doi.org/10.14348/molcells.2016.2368.

[48] P.A. Karplus, A primer on peroxiredoxin biochemistry, Free Radic. Biol. Med. 80 (2015) 183–190, http://dx.doi.org/10.1016/j.freeradbiomed.2014.10.009.

[49] E. Daugas, S.A. Susin, N. Zamzami, K.F. Ferri, T. Irinopoulou, N. Larochette, M.C. Prévost, B. Leber, D. Andrews, J. Penninger, G. Kroemer, Mitochondrio-nuclear translocation of AIF in apoptosis and necrosis, FASEB J. 14 (2000) 729–739.

[50] D. Munro, J.R. Treberg, A radical shift in perspective: mitochondria as regulators of reactive oxygen species, J. Exp. Biol. 220 (2017) 1170–1180, http://dx.doi.org/10.1242/jeb.132142.

[51] G.A. Stepanov, J.A. Filippova, A.B. Komissarov, E.V. Kuligina, V.A. Richter, D.V. Semenov, Regulatory role of small nucleolar RNAs in human diseases, BioMed Res. Int. (2015) 206849, http://dx.doi.org/10.1155/2015/206849.

[52] T.M. Carlile, M.F. Rojas-Duran, B. Zinshteyn, H. Shin, K.M. Bartoli, W.V. Gilbert, Pseudouridine profiling reveals regulated mRNA pseudouridylation in yeast and human cells, Nature 515 (2014) 143–146, http://dx.doi.org/10.1038/nature13802.

[53] G. Tortoriello, J.F. de Celis, M. Furia, Linking pseudouridine synthases to growth, development and cell competition, FEBS J. 277 (2010) 3249–3263, http://dx.doi.org/10.1111/j.1742-4658.2010.07731.x.

[54] R. Vicidomini, A. Di Giovanni, A. Petrizzo, L.F. Iannucci, G. Benvenuto, A.C. Nagel, A. Preiss, M. Furia, Loss of Drosophila pseudouridine synthase triggers apoptosis-induced proliferation and promotes cell-nonautonomous EMT, Cell Death Dis. 6 (2015) e1705, http://dx.doi.org/10.1038/cddis.2015.68.

[55] R. Vicidomini, A. Petrizzo, A. Di Giovanni, L. Cassese, A.A. Lombardi, C. Pragliola, M. Furia, Drosophila dyskerin is required for somatic stem cell homeostasis, Sci. Rep. 7 (2017) 347, http://dx.doi.org/10.1038/s41598-017-00446.

[56] P. Sancho, D. Barneda, C. Heeschen, Hallmarks of cancer stem cell metabolism, Br. J. Cancer 114 (2016) 1305–1312, http://dx.doi.org/10.1038/bjc.2016.152.

[57] V. Stresing, E. Baltziskueta, N. Rubio, J. Blanco, M.C. Arriba, J. Valls, M. Janier, P. Clézardin, R. Sanz-Pamplona, C. Nieva, M. Marro, D. Petrov, N. Sierra, Peroxiredoxin 2 specifically regulates the oxidative and metabolic stress response of human metastatic breast cancer cells in lungs, Oncogene 32 (2013) 724–735, http://dx.doi.org/10.1038/onc.2012.93.

[58] W. Lu, Z. Fu, H. Wang, J. Feng, J. Wei, J. Guo, Peroxiredoxin 2 is upregulated in colorectal cancer and contributes to colorectal cancer cells' survival by protecting cells from oxidative stress, Mol. Cell. Biochem. 387 (2014) 261–270, http://dx.doi.org/10.1007/s11010-013-1891-4.

[59] W. De Haes, L. Frooninckx, R. Van Assche, A. Smolders, G. Depuydt, J. Billen, B.P. Braeckman, L. Schoofs, L. Temmerman, Metformin promotes lifespan through mitohormesis via the peroxiredoxin PRDX-2, Proc. Natl. Acad. Sci. USA 111 (2014) E2501–E2509, http://dx.doi.org/10.1073/pnas.1321776111.

[60] M. Eisenberg-Bord, M. Schuldiner, Ground control to major TOM: mitochondria-nucleus communication, FEBS J. 284 (2017) 196–210, http://dx.doi.org/10.1111/febs.13778.

[61] G. Saretzki, Extra-telomeric functions of human telomerase: cancer, mitochondria and oxidative stress, Curr. Pharm. Des. 20 (2014) 6386–6403.